Monthly Notices
of the
ROYAL ASTRONOMICAL SOCIETY

MNRAS **496,** 875–887 (2020)
Advance Access publication 2020 June 4

doi:10.1093/mnras/staa1546

The ALPINE–ALMA [C II] Survey: on the nature of an extremely obscured serendipitous galaxy

M. Romano [1,2]★ P. Cassata [1,2] L. Morselli [1,2] B. C. Lemaux [3] M. Béthermin [4] P. Capak [5,6,7] A. Faisst [5] O. Le Fèvre [4] D. Schaerer [8,9] J. Silverman [10,11] L. Yan [12] S. Bardelli [13] M. Boquien [14] A. Cimatti,[15,16] M. Dessauges-Zavadsky [8] A. Enia [1,2] Y. Fudamoto [8] S. Fujimoto [6,17] M. Ginolfi [8] C. Gruppioni [13] N. P. Hathi [18] E. Ibar,[19] G. C. Jones [20,21] A. M. Koekemoer [18] F. Loiacono [13,15] C. Mancini [1] D. A. Riechers,[22,23] G. Rodighiero [1,2] L. Rodríguez-Muñoz [1] M. Talia [13,15] L. Vallini [24] D. Vergani,[13] G. Zamorani [13] and E. Zucca [13]

Affiliations are listed at the end of the paper

Accepted 2020 May 27. Received 2020 May 26; in original form 2020 January 31

ABSTRACT

We report the serendipitous discovery of a dust-obscured galaxy observed as part of the Atacama Large Millimeter Array (ALMA) Large Program to INvestigate [C II] at Early times (ALPINE). While this galaxy is detected both in line and continuum emissions in ALMA Band 7, it is completely dark in the observed optical/near-infrared bands and only shows a significant detection in the UltraVISTA K_s band. We discuss the nature of the observed ALMA line, that is [C II] at $z \sim 4.6$ or high-J CO transitions at $z \sim 2.2$. In the first case, we find a [C II]/FIR luminosity ratio of $\log(L_{[\mathrm{C\,II}]}/L_{\mathrm{FIR}}) \sim -2.5$, consistent with the average value for local star-forming galaxies (SFGs). In the second case instead, the source would lie at larger CO luminosities than those expected for local SFGs and high-z submillimetre galaxies. At both redshifts, we derive the star formation rate (SFR) from the ALMA continuum and the physical parameters of the galaxy, such as the stellar mass (M_*), by fitting its spectral energy distribution. Exploiting the results of this work, we believe that our source is a 'main-sequence', dusty SFG at $z = 4.6$ (i.e. [C II] emitter) with $\log(\mathrm{SFR}/\mathrm{M}_\odot\,\mathrm{yr}^{-1}) \sim 1.4$ and $\log(M_*/\mathrm{M}_\odot) \sim 9.9$. As a support to this scenario our galaxy, if at this redshift, lies in a massive protocluster recently discovered at $z \sim 4.57$, at only $\sim$1 proper Mpc from its centre. This work underlines the crucial role of the ALPINE survey in making a census of this class of objects, in order to unveil their contribution to the global SFR density at the end of the Reionization epoch.

Key words: galaxies: evolution – galaxies: high-redshift.

1 INTRODUCTION

The last decades have seen dramatic advances in our knowledge of galaxy formation and evolution (e.g. Giavalisco 2002; Renzini 2006; Silk & Mamon 2012; Carilli & Walter 2013; Madau & Dickinson 2014; Naab et al. 2017). The global star formation rate density (SFRD) has been found to rise during the cosmic reionization from $z \sim 10$, peak at $1 < z < 3$, and finally decrease by a factor of $\sim$10 to the local Universe (Lilly et al. 1996; Bouwens et al. 2011; Madau & Dickinson 2014). Several studies suggest that, at all epochs, the bulk of the star formation activity takes place in galaxies lying on the 'main sequence' (MS): a tight correlation between the star formation rate (SFR) and the stellar mass (M_*, Daddi et al. 2007; Rodighiero et al. 2011; Speagle et al. 2014; Santini et al. 2017). Therefore, we have indications that most of the stars in the Universe formed along the MS, at the peak of the SFRD at $z \sim 2$. However, we are still trying to understand which are the main mechanisms responsible for the rapid increase of the SFRD at $z < 6$. One possible explanation is an increase in the gas fraction along with a rising in the star formation efficiency per unit mass, possibly driven by galaxy mergers (Genzel et al. 2015; Silverman et al. 2015; Scoville et al. 2016).

At $z > 3$, the cosmic SFRD is almost exclusively constrained by ultraviolet (UV)-selected samples (Bouwens et al. 2012a,b;

★ E-mail: michael.romano@studenti.unipd.it

Schenker et al. 2013; Oesch et al. 2015), lacking information about the star formation obscured by the dust. Rest-frame UV-selected galaxies must be corrected for the dust absorption: wrong dust corrections can lead to large uncertainties on the SFR estimates and, consequently, to an incorrect picture of the star formation history (SFH) of the Universe (e.g. Gallerani et al. 2010; Castellano et al. 2014; Scoville et al. 2015; Álvarez-Márquez et al. 2016). At the same time, heavily dust-obscured star-forming galaxies (SFGs) may be completely missed by surveys probing the rest-frame UV/optical emissions.

With the advent of new facilities, such as the Atacama Large Millimeter Array (ALMA), a population of faint and dusty SFGs has been confirmed at high redshift, for example submillimetre galaxies (SMGs, Dunlop et al. 2004; Daddi et al. 2009; Riechers et al. 2010; Huang et al. 2014; Simpson et al. 2014; Santini et al. 2016; Cooke et al. 2018), ALMA-only sources (e.g. Williams et al. 2019), the extremely red objects selected with *H* and Infrared Array Camera (IRAC) colours (HIEROs galaxies) from Wang et al. (2016). While the bulk of these objects peaks at $2 < z < 3$, a significant tail of dusty galaxies without optical/near-infrared (NIR) detections appears to be in place at $z > 4$ (Capak et al. 2008; Daddi et al. 2009; Riechers et al. 2010; Walter et al. 2012; Riechers et al. 2013; Simpson et al. 2014; Cooke et al. 2018; Pavesi et al. 2018; Dudzevičiūtė et al. 2020).

In particular, a large population of high-redshift SMGs has been discovered during the last years. For instance, Walter et al. (2012) combined measurements from the IRAM Plateau de Bure Interferometer and the Jansky Very Large Array to put constraints on the dust-obscured starburst HDF850.1, one of the first galaxies completely obscured in the observed optical/NIR wavelengths and identified in the submillimetre band. This source is at $z_{\rm spec} = 5.18$ among an overdensity of galaxies at the same redshift, with a [C II]/FIR luminosity ratio comparable to that observed in local SFGs. Moreover, many of these objects are extreme starbursts, such as HFLS3. This source is confirmed to be at $z_{\rm spec} = 6.34$ exploiting information from different molecular and atomic fine structure cooling lines and shows a large FIR luminosity (i.e. $L_{\rm FIR} \sim 2 \times 10^{13}$ L$_\odot$) and SFR $>10^3$ M$_\odot$ yr^{-1} (Riechers et al. 2013). Simpson et al. (2014) analysed a sample of 96 SMGs from the ALMA–LABOCA Chandra Deep Field-South Survey (Hodge et al. 2013), finding a median photometric redshift of $z_{\rm phot} \sim 2.5$, with 35 per cent of the SMGs lying at $z > 3$ (and ∼20 sources most likely at $z > 4$). Cooke et al. (2018) examined the ALMA data cubes of ∼700 high-redshift SMGs from the ALMA-SCUBA-2 survey of the Ultra Deep Survey (UDS) field (AS2UDS), searching for serendipitous emission lines. They found 10 candidate line emitters, 8 of which are likely [C II] emitters at $z \sim 4.5$ and with the remaining two sources associated with high-*J* CO emission. Dudzevičiūtė et al. (2020) found that ∼17 per cent of the SMGs in the AS2UDS survey are undetected in the observed optical/NIR bands and fainter than $K \sim 25.7$. These sources preferentially lie at higher redshifts ($z > 3$) with respect to the median photometric redshift of the sample, that is $z_{\rm phot} \sim 2.6$. An in-depth study of this elusive population of galaxies is necessary in order to complete the census of the SFGs at high redshift contributing to the cosmic SFH as well as to better understand the early phases of the galaxy formation (e.g. Blain et al. 2002; Casey, Narayanan & Cooray 2014).

In this context, the ALMA Large Program to INvestigate [C II] at Early times (ALPINE, Faisst et al. 2019; Le Fèvre et al. 2019; Béthermin et al. 2020) is going to improve our knowledge of the obscured star formation at $z > 4$. It takes advantage of the observations of the singly ionized carbon [C II] at 158 μm and its adjacent FIR continuum for a sample of 118 SFGs in the Cosmic Evolution Survey (COSMOS, Scoville et al. 2007a,b) and the Extended Chandra Deep Field South (Giavalisco et al. 2004; Cardamone et al. 2010) fields. These sources are spectroscopically confirmed to be at $4 < z < 6$ with the Visible Multi-Object Spectrograph at the Very Large Telescope (VLT; Le Fèvre et al. 2003, 2015) and with the DEep Imaging Multi-Object Spectrograph (DEIMOS) at the Keck II telescope (Faber et al. 2003; Hasinger et al. 2018).

The [C II] line is one of the strongest lines in the FIR band (e.g. Stacey et al. 1991) as it is one of the main coolants of the interstellar medium (ISM; Carilli & Walter 2013). Since it has a lower ionization potential than neutral hydrogen (H I), that is 11.3 eV compared to 13.6 eV, this line can trace different gas phases, such as dense photodissociation regions (PDRs; Hollenbach & Tielens 1999), neutral diffuse gas (e.g. Wolfire et al. 2003; Vallini et al. 2015), and diffuse ionized gas (e.g. Cormier et al. 2012). In principle, in order to remove the ambiguity on the interpretation of the [C II] emission, the relative contribution of the various gas phases should be assessed. However, different studies suggest that the bulk of the [C II] emission arises from the external layers of molecular clouds heated by UV photons in the PDRs (Stacey et al. 1991; Madden et al. 1997; Kaufman et al. 1999; Cormier et al. 2015; Pavesi et al. 2016); thus, this line can be used as a tracer of star formation (e.g. De Looze et al. 2014; but see also Zanella et al. 2018 who suggest that [C II] is a better tracer of the molecular gas). Therefore, the combination of the FIR continuum and of the UV measurements, together with the [C II] observations, will provide an estimate of the total (obscured and unobscured) star formation in these galaxies at the redshift explored by the ALPINE survey. This corresponds to the 80–95 per cent of the cosmic SFRD at $4 < z < 6$ (Casey et al. 2012; Bouwens et al. 2016; Capak et al. 2015; Aravena et al. 2016; Novak et al. 2017). The remaining 5–20 per cent of the star formation is yielded by a free blind survey covering an additional area of 25 arcmin^2 beyond the rest-frame UV-selected ALPINE targets, where many galaxies have been serendipitously detected so far (Loiacono et al. 2020). Among these, different sources are completely obscured in the observed optical/NIR bands. The study of these objects is crucial for obtaining a robust estimate of the total SFRD at $z > 4$ and for characterizing the overall population of the high-redshift SFGs.

In this work, we discuss the nature of a galaxy (hereafter, Gal−A) randomly discovered in the field of the ALPINE target DEIMOS_COSMOS_665626 (hereafter, DC_665626). The galaxy has a spatial offset of ∼6 arcsec (1 arcsec is ∼7 kpc at $z = 4.583$, the redshift of the target) from DC_665626. It does not show any optical counterpart at the position of the emission detected with ALMA and, for this reason, its nature results to be ambiguous. Besides, since Gal−A is the brightest galaxy detected in line emission among all those having no optical counterpart and serendipitously observed in ALPINE so far (Loiacono et al. 2020), this work can be exploited as a benchmark for future analysis on this type of source.

The paper is organized as follows: in Section 2 we introduce the available data we have for Gal−A and explain the methods used to analyse this source. We present the results in Section 3 and discuss them in Section 4, trying to constrain the nature of the galaxy. Summary and conclusions are provided in Section 5.

Throughout this paper, we assume a Λ-cold dark matter cosmology with $H_0 = 70$ km s^{-1} Mpc^{-1}, $\Omega_{\rm m} = 0.3$, and $\Omega_\Lambda = 0.7$ (Planck Collaboration 2018). We furthermore use a Chabrier (2003) initial mass function (IMF) and AB magnitudes.

2 OBSERVATIONS AND DATA REDUCTION

2.1 ALMA data

DC_665626 was observed with ALMA in Band 7 ($\nu_{\rm obs}$ = [275–373] GHz) on 2018 May 25 (Cycle 5; Project 2017.1.00428.L, PI: O. Le Fèvre) using 45 antennas with the C43-2 array configuration (with a maximum baseline of ∼ 250 m). The on-source integration time was 16 min, with a total elapsed time of 37 min.

The spectral setup consisted of two sidebands with a frequency range of $\Delta^{\rm l}_{\nu} \simeq [339 - 343]$ GHz and $\Delta^{\rm u}_{\nu} \simeq [351 - 355]$ GHz for the lower and upper sidebands, respectively. Both sidebands were made up of two spectral windows (SPWs) of width 1.875 GHz, each of which containing 128 channels 15.625 MHz wide (the sidebands overlapped for seven channels), with a typical rms of 0.6 mJy beam^{-1} per channel. The flux and phase were calibrated using the standard calibrators J1058+0133 and J0948+0022, respectively.

The data are analysed using standard pipelines for ALMA reduction included in the software CASA (McMullin et al. 2007), version 5.4.0. The imaging is obtained by running the TCLEAN task on the visibilities, setting a threshold of $3\sigma_{\rm rms}$ on the noise level when cleaning the data (where $\sigma_{\rm rms}$ is obtained from the dirty image), and with a natural weighting scheme to increase the sensitivity.

2.2 Identification of the serendipitous source

As part of the COSMOS field (Scoville et al. 2007a,b), which is one of the most thoroughly studied regions of the sky so far, multiwavelength data are available for the whole ALPINE sample, including high-resolution *Hubble Space Telescope* (*HST*) imaging (Koekemoer et al. 2007, 2011) and photometry from the Canada–France–Hawaii Telescope (CFHT), the *Spitzer* telescope, and other facilities (Capak et al. 2007; Laigle et al. 2016). Spectroscopic redshifts are available from large optical spectroscopic campaigns at the VLT (VUDS; Le Fèvre et al. 2015) and Keck (DEIMOS 10k survey; Hasinger et al. 2018). Multiband photometry and spectroscopic data allow us to build spectral energy distributions (SEDs) and to derive robust physical parameters including SFRs and stellar masses through SED-fitting (Faisst et al. 2019). As a result of this analysis, we find that DC_665626 has $\log(M_*/{\rm M}_\odot) = 9.21^{+0.16}_{-0.18}$, $\log({\rm SFR}/[{\rm M}_\odot\,{\rm yr}^{-1}]) = 0.71^{+0.29}_{-0.18}$, and a spectroscopic redshift of $z_{\rm spec} = 4.583$, obtained from the Lyα emission and the ISM absorption lines in the observed-frame optical spectrum.

Since the ALPINE target DC_665626 is at $z_{\rm spec} = 4.583$, the [C II] emission from this source ($\nu_{\rm rest} = 1900.54$ GHz) is expected to be redshifted at around $\nu_{\rm obs} = 340.42$ GHz, falling inside the lower sideband of the observed ALMA spectrum. When we inspect the data cube, together with the [C II] emission coming from DC_665626 (at 4.4σ, Béthermin et al. 2020), we identify a more significant line emission feature with a spatial offset of ∼6 arcsec (∼40 proper kpc at $z \sim 4.6$) with respect to the ALPINE target. We refer to the source of this emission as Gal−A (RA: 10:01:13.82, Dec.: +02:18:40.66), that is detected both in continuum and in line emissions at 5σ and 12σ, respectively. Fig. 1 shows the continuum-subtracted moment-0 map of Gal−A. This is computed by summing the integrated intensity in all the spectral channels in the data cube containing the line emission, that is $M(x, y) = \sum_{i=1}^{N_{\rm channel}} S_\nu(x, y, i)\Delta {\rm v}_{\rm channel}(i)$, where $S_\nu(x, y, i)$ is the flux density in the ith channel at the position (x,y) and $\Delta v_{\rm channel}$ is the velocity width of the ith channel (see Section 2.4 fore more details).

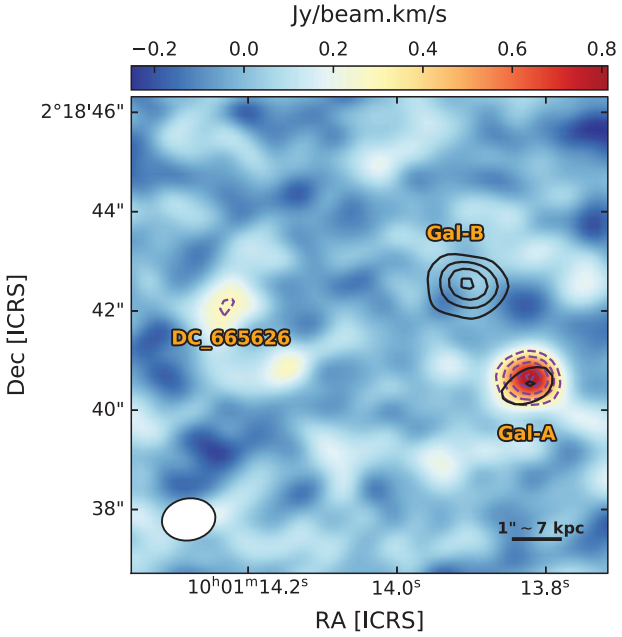

Figure 1. Continuum-subtracted moment-0 map of Gal−A. The ALPINE target DC_665626, Gal−A and Gal−B are labelled. Line and continuum emissions are shown with dashed violet and solid black contours starting from 4σ and 3σ (at step of 2σ), respectively. The white ellipse in the bottom left corner is the synthesized beam.

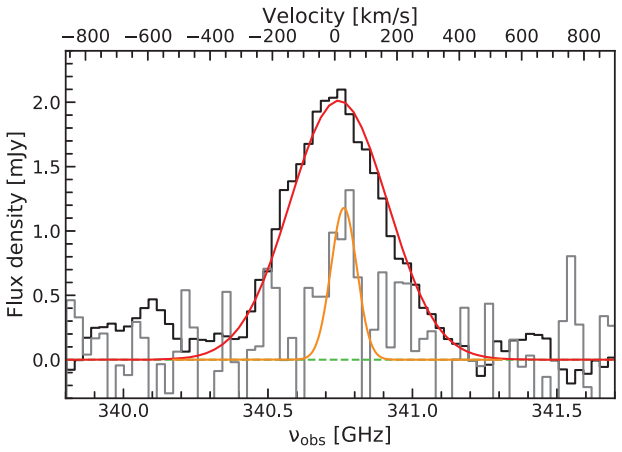

Figure 2. Emission line flux at the position of Gal−A (black histogram) as a function of the observed frequency. The solid red curve represents the Gaussian fit on the line. The dashed green line marks the zero-flux level. The velocity offset is reported on the top axis. For comparison, we also show the spectrum of the [C II] line arising from DC_665626 (grey histogram) with its associated Gaussian fit (solid orange curve).

The synthesized beam with a size of 1.08 arcsec × 0.85 arcsec at PA = −80° and another galaxy (hereafter, Gal−B) detected at 9σ in continuum only northwards of the offset emission (∼2 arcsec away from Gal−A when considering the peak positions of the two emissions) are also displayed.

We show in Fig. 2 the spectrum of the emission line observed at the position of Gal−A (black histogram). It is extracted from a circular region 2 arcsec wide, including the 2σ contours from the moment-0 map of the source. Using the *spectral profile tool* within the CASA viewer, we fit the line profile with a Gaussian

function finding a full width at half-maximum ($FWHM_{line}$) of 308 ± 34 km s^{-1} and a peak frequency at $\nu_{peak} = 340.76$ GHz. For comparison, we also show the [C II] line spectrum (grey histogram) of the main ALPINE target, obtained in the same way as for Gal−A.

Though DC_665626 is detected in [C II] in spatial coincidence with its rest-frame UV emission, we consider the possibility that the emission centred at the position of Gal−A is connected with that of the ALPINE target. The displacement between [C II] and UV/Lyα emission has already been observed in high-redshift galaxies (Gallerani et al. 2012; Willott et al. 2015; Cassata et al. 2020; but see also Bradač et al. 2017). It is also reproduced by radiative transfer simulations as a consequence of the strong stellar feedback which could quench the [C II] emission in the central region of the galaxies, allowing it to arise mostly from infalling or satellite clumps of neutral gas around them (Vallini et al. 2013; Maiolino et al. 2015). However, these models predict spatial offsets up to ∼1–2 arcsec (∼7–14 kpc at the redshift of the target), well below the offset that we measure in this case ($\gtrsim$6 arcsec). Therefore, we exclude that the observed ALMA emission at the position of Gal−A is directly linked to DC_665626.

2.3 Multiwavelength photometry of Gal−A

As Gal−A lies in the COSMOS field (Laigle et al. 2016), we exploit all the available multiwavelength photometry in order to identify the counterpart associated with the discovered emission. In Fig. 3, we present some cutouts centred on this galaxy in different photometric filters, from the UV to the FIR. Gal−B is visible in most of the photometric bands and has a photometric redshift $z_{phot} = 2.25^{+0.22}_{-0.15}$, as reported in the COSMOS2015 catalogue (Laigle et al. 2016). Another foreground galaxy, labelled Gal−C in Fig. 3, is well detected in the images from the optical to the NIR wavelengths and has $z_{phot} = 2.02^{+0.12}_{-0.12}$, from COSMOS2015. Conversely, Gal−A is not clearly identified in any optical filter. It is fairly visible in the UltraVISTA K_s band, even if it is not listed as a detection in the UltraVISTA DR4 catalogue (McCracken et al. 2012).

More in detail, to reproduce the SED of Gal−A, we use observations in the u^* band from MegaCam on CFHT, as well as the g, r, i and z filters from the Hyper Suprime-Cam (HSC) on the *Subaru* telescope, in order to set an upper limit to the optical emission of the source. NIR constraints come from the Y, J, H, and K_s bands from the VISTA InfraRed CAMera (VIRCAM) on the VISTA telescope. Finally, we obtain information on the SED up to ∼8 μm in the observed frame from the IRAC channels on *Spitzer*. For each band, we centre a fixed aperture of 1.4 arcsec of diameter on Gal−A (enclosing the 3σ contours of the emission line detected by ALMA) and estimate its flux. We then compute the limiting magnitude as the standard deviation of the fluxes measured in 10 000 apertures (of 1.4 arcsec of diameter) randomly distributed in a wide region of the sky (masked for the emission of bright sources) and assume it as the error on the flux. As expected, we do not find any significant detection (>5σ) of our source in the optical filters. For this reason, we consider the measured 5σ limiting magnitudes as upper limits in these bands. The same argument applies to the VISTA filters except for the K_s band in which, as mentioned above, a faint emission arises at the position of Gal−A. Making use of SExtractor (Bertin & Arnouts 1996), we manage to deblend the analysed galaxy from the other two nearby sources obtaining an estimate of its apparent magnitude in this band. Through this analysis, Gal−A is detected at ∼8.3σ with an AB magnitude $K_s = (24.4 \pm 0.1)$, which is very close to the 5σ limiting magnitude of ∼24.5 (computed in 2.0 arcsec diameter apertures) from the UltraVISTA DR4 catalogue. It is worth noting that in this case we do not assume the uncertainty on the flux resulting from SExtractor. We consider instead the corresponding 1σ limiting magnitude as the error on the flux as done for the other bands though, in practice, the two uncertainty estimates are comparable.

Finally, a weak emission seems to arise at the position of Gal−A in the IRAC bands. However, as shown in Fig. 3, this could be partially contaminated by the emission of the two nearby galaxies at $z_{phot} \sim 2$ in the 3.6 and 4.5 μm bands, while it seems to emerge from the background at 8.0 μm, where Gal−B and Gal−C become fainter. We find that, in the *Rainbow* catalogue (Pérez-González et al. 2008; Barro et al. 2011a,b), Gal−B and Gal−C have been deblended in all the four IRAC channels using the *Subaru r* band as a prior for the two sources, while no counterpart of Gal−A is present. We briefly summarize here the main steps of the deblending procedure adopted in Barro et al. (2011a,b). At first, several catalogues are cross-correlated to the IRAC 3.6 + 4.5 μm source position using a 2 arcsec search radius, in order to identify the associated counterpart in the available bands. When multiple counterparts lying at least 1 arcsec away (half of the typical IRAC point spread function, i.e. PSF ∼ 2 arcsec) from each other are found in the optical/NIR images, the deblending procedure is applied. The PSF of the higher resolution image (in our case, the *Subaru r* band) is convolved with the IRAC PSF to create a model image. Then, the intensity of each source is scaled to match the flux measured on the IRAC image in 0.9 arcsec radii centred on the positions of the optical counterparts. At the end, total magnitudes are computed applying aperture corrections in each IRAC band. For more details on the deblending procedure and on the counterparts identification, see Barro et al. (2011a,b), and references therein.

In a similar way, we attempt a deblending procedure on Gal−A using the 2D GALFIT fitting algorithm (Peng et al. 2002) in order to extract the photometric information on this object from the IRAC bands. We model Gal−B and Gal−C as point-like sources, using their optical positions and deblended fluxes from *Rainbow* as a first guess, and considering for each IRAC channel its typical PSF. To obtain the flux in each channel, we perform aperture photometry at the position of Gal−A in the residual maps.[1] We are aware that with this procedure we may underestimate the flux of Gal−A in the IRAC channels as we are spreading the global flux of the three components on only two sources. To account for this, when performing SED fitting (see Section 3.2), we decide to consider the IRAC fluxes ranging between the deblended (lower) and blended (higher) values. We find, however, that our conclusions do not depend on this assumption; in fact, we obtain similar results when using the deblended fluxes in the SED fitting. As an alternative approach, we try to fit a three-components model leaving as a free parameter the flux corresponding to Gal−A and using the ALMA continuum peak position as a prior. However, probably due to the small distance between the galaxies, the code is not able to perform the fit. Table 1 summarizes the photometric information we obtain for Gal−A; this is exploited in Section 3.2 to estimate the physical properties of this galaxy from the SED fitting.

[1] As we use a fixed aperture of 1.4 arcsec of diameter (which is smaller than the typical PSF of the IRAC channels), we compute aperture corrections from point-source objects lying in the field of our galaxy, in order to estimate the total fluxes in the IRAC filters. In particular, we divide the flux measured in these bands by 0.28, 0.30, 0.29, and 0.19, going from 3.6 to 8.0 μm.

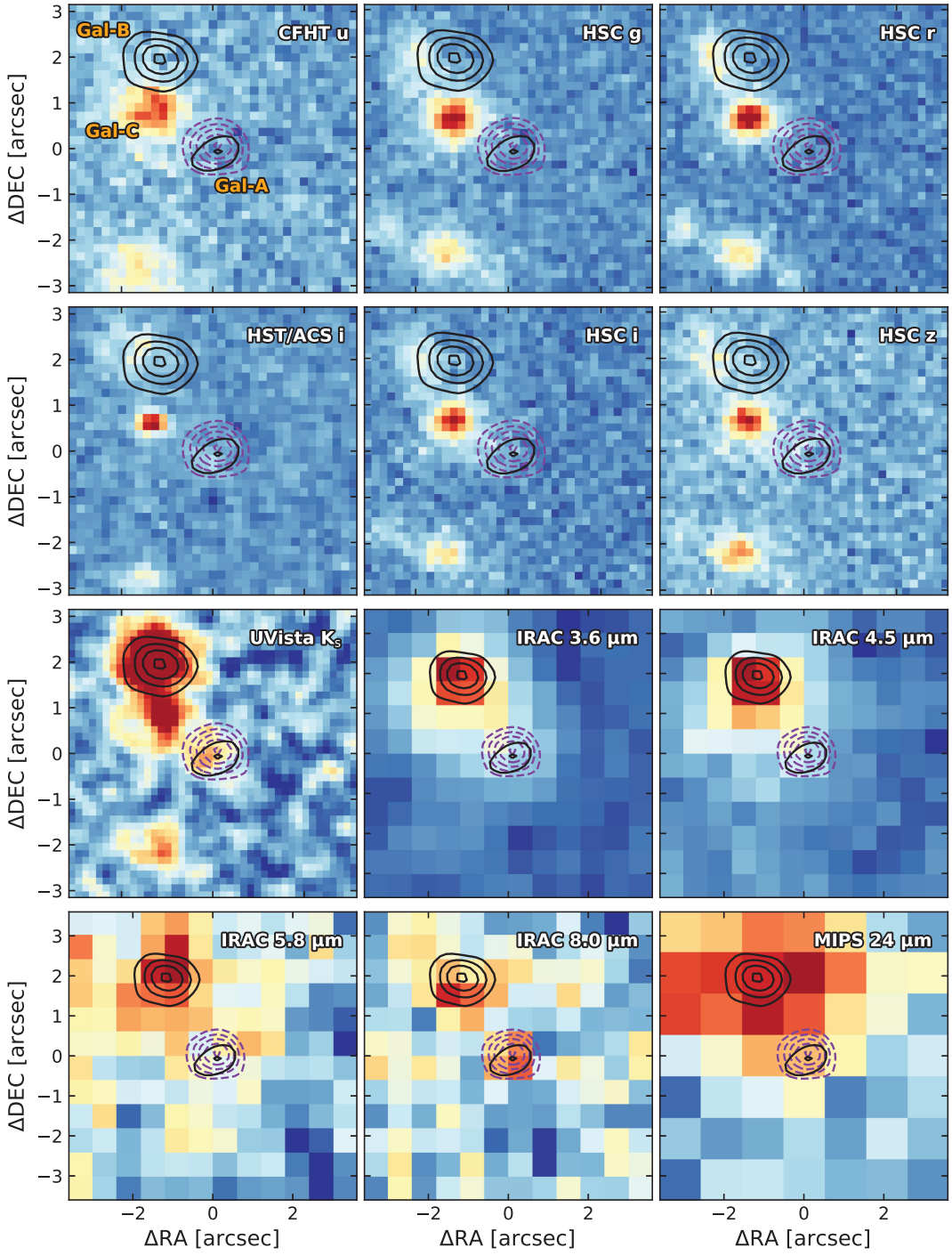

Figure 3. Cutouts centred on Gal−A in different photometric filters, from *HST*/ACS (Koekemoer et al. 2007) and *Subaru*, UltraVISTA, and *Spitzer* (Capak et al. 2007; Laigle et al. 2016). The violet dashed and black solid contours are $>3\sigma$ line and continuum emissions (at steps of 2σ), respectively. Gal−A, Gal−B, and Gal−C are labelled in the upper left plot of the figure. Wavelengths increase from the upper left to the bottom-right corner.

2.4 Analysis of the serendipitous source

Since Gal−A shows no optical counterpart, we do not know a priori the nature of the emission line; it could be [C II] emission at a similar redshift of DC_665626 (i.e. $z_{\rm spec} = 4.583$), but also high-J CO transitions are expected ($J_{\rm up} > 3$) at the observed frequencies in ALMA Band 7, although at lower redshift (Carilli & Walter 2013).

In this work, we consider only the two high-J CO transitions with $J_{\rm up} = 9$, 10 which fall into the SPW of observation at $z \gtrsim 2$. Indeed, Ilbert et al. (2013) claim that galaxies at $z < 2$ (corresponding in our case to lower CO transitions) should be more easily detected in the UV/optical filters, with more than the 95 per cent of the sources detected in at least four photometric bands, from the UV to the NIR (Ilbert et al. 2006). Therefore, if our source was at $z < 2$, we would expect it to be visible in the optical bands shown in Fig. 3.

For these reasons, in this work we discuss the nature of Gal−A considering three transitions as possible interpretations for the

Table 1. Summary of available data for Gal−A in each photometric band used for the SED fitting (see Section 3.2). The first two columns are the instruments (with relative telescopes) and filters used. Central wavelength is the mean wavelength weighted by the transmission of the filter. In the last column we report the 5σ upper limits for all the bands from the UV to the NIR, except for the K_s detection which is obtained with SExtractor. For the IRAC channels, we report the upper limits obtained by measuring the flux at the position of Gal−A before the deblending procedure (see the text). All the flux measurements are computed in apertures of 1.4 arcsec of diameter.

Instrument /Telescope	Filter	Central λ (μm)	Observed flux (μJy)
MegaCam/CFHT	u^*	0.3811	$<4.72 \times 10^{-2}$
HSC/*Subaru*	g	0.4816	$<3.50 \times 10^{-2}$
	r	0.6234	$<4.79 \times 10^{-2}$
	i	0.7741	$<7.24 \times 10^{-2}$
	z	0.8912	$<1.04 \times 10^{-1}$
VIRCAM /VISTA	Y	1.0224	$<3.28 \times 10^{-1}$
	J	1.2556	$<3.98 \times 10^{-1}$
	H	1.6499	$<5.40 \times 10^{-1}$
	K_s	2.1578	$(6.31 \pm 0.76) \times 10^{-1}$
IRAC/*Spitzer*	ch1	3.5573	<2.40
	ch2	4.5049	<2.67
	ch3	5.7386	<3.59
	ch4	7.9274	<10.11

observed emission: [C II] at $\nu_{\rm rest} = 1900.5$ GHz, CO(9−8) at $\nu_{\rm rest} = 1036.9$ GHz, and CO(10−9) at $\nu_{\rm rest} = 1152.0$ GHz. As the observed emission line has a peak frequency of 340.76 GHz, Gal−A would be at redshift $z_{\rm gal} = 4.577$, 2.043, and 2.381 for [C II], CO(9−8), and CO(10−9), respectively. Table 2 lists the considered transitions and their rest frequencies, as well as the corresponding redshift for Gal−A in the three cases.

To estimate the intensity of the line and continuum emissions from Gal−A, we separate these components using the CASA IMCONTSUB task. Giving in input all the channels in the SPWs free of the emission line, this task creates a continuum map of the source and a continuum-subtracted data cube. We then select all the consecutive channels having emission above $1\sigma_{\rm spec}$ (i.e. the rms estimated from the line spectrum) encompassing the emission line in order to compute the moment-0 map with the CASA IMMOMENTS task.

The line and continuum fluxes are computed using the CASA IMFIT task. We define a region surrounding the emissions and then select only the pixels with a flux density larger than 2σ. As the size of the emission region is comparable with the clean beam size, we assume that the source is unresolved and we take the peak flux as the total flux. We obtain $S_{\rm cont} = 245 \pm 24$ μJy and $S_{\rm line}\Delta v = 1.19 \pm 0.11$ Jy km s^{-1} for the continuum and the line, respectively.

We derive the total infrared (between 8 and 1000 μm) luminosity of the source, in the three cases, assuming a shape of its SED from Magdis et al. (2012) and normalizing its flux to $S_{\rm cont}$, which is the observed flux at ∼845–880 μm. According to Kennicutt (1998), this luminosity also provides a good estimate of the obscured SFR. We obtain $\log(L_{\rm FIR}/{\rm L}_\odot) = 11.38 \pm 0.5$ in case of [C II] emission, $\log(L_{\rm FIR}/{\rm L}_\odot) = 11.44 \pm 0.5$ for CO(9−8) and $\log(L_{\rm FIR}/{\rm L}_\odot) = 11.42 \pm 0.5$ for CO(10−9) emissions. The uncertainties on the FIR luminosities are calculated by adding in quadrature the error on the continuum flux (∼0.04 dex, which directly affects the $L_{\rm FIR}$ estimates) and a conservative systematic error of 0.5 dex which takes into account possible variations in the luminosity caused by different SED templates (e.g. Capak et al. 2015; Casey et al. 2018). As can be seen, this latter term dominates over the uncertainty on the continuum flux. Following equation (4) in Kennicutt (1998), these FIR luminosities translate into SFRs[2] ranging from 24 to 28 $M_\odot$ yr^{-1}. Finally, we estimate the line luminosities as in Solomon, Downes & Radford (1992) using the following relation:

$$L_{\rm line} = 1.04 \times 10^{-3}\, S_{\rm line}\, \Delta v\, D_L^2\, \nu_{\rm obs}\, [{\rm L}_\odot], \quad (1)$$

where D_L is the luminosity distance of the source in Mpc and $\nu_{\rm obs}$ the observed peak frequency in GHz. We thus obtain $\log(L_{\rm [C\,II]}/{\rm L}_\odot) = 8.88 \pm 0.04$, $\log(L_{\rm CO}/{\rm L}_\odot) = 8.04 \pm 0.04$ for CO(9−8) and $\log(L_{\rm CO}/{\rm L}_\odot) = 8.20 \pm 0.04$ for CO(10−9), where the uncertainties are computed by propagating the line flux error on equation (1). All the above-mentioned physical quantities computed for Gal−A are reported in Table 2.

3 RESULTS

3.1 On the nature of the serendipitous source

With no detections in the optical bands and with the only information of the ALMA Band 7 line and continuum, unveiling the nature of Gal−A is a challenging task. We use here the physical quantities estimated in Section 2.4 to deduce plausible conclusions on our source.

Fig. 4 (left-hand panel) shows the correlation between $L_{\rm CO}$ (for the (9−8) and (10−9) transitions) and $L_{\rm FIR}$ for a compilation of SFGs in the literature, together with the expected position of Gal−A. The respective best-fitting lines on the individual data are also shown (solid lines, Liu et al. 2015). It is worth noting that the reported values are for local galaxies, spanning an FIR luminosity range between ∼10^8–10^{12} $L_\odot$. However, the empirical correlations continue to apply even including high-redshift galaxies (filled circles in the figure). In this case indeed, as shown in Liu et al. (2015), the results of the fit do not significantly change. We then note that the computed $L_{\rm FIR}$ by Liu et al. (2015) are integrated between 40 and 400 μm, which is a smaller wavelength range with respect to the one adopted in this paper to compute $L_{\rm FIR}$. In order to take this difference into account, we rescale the FIR luminosities of Gal−A in Fig. 4 to the same integration interval as in Liu et al. (2015), for consistency ($L_{\rm FIR}^{8-1000}/L_{\rm FIR}^{40-400} \sim 1.4$, on average). It can be seen that, for both possible CO transitions, our galaxy would be an outlier of the empirical relations found by Liu et al. (2015), if it was at $z \sim 2$. However, considering the large uncertainties on $L_{\rm FIR}$ (i.e. 0.5 dex), Gal−A could still be part of the lower envelope of local SFGs in the figure, tracing high-density regions ($n_{\rm H2,\,crit} \sim 10^5$–$10^6$ cm^{-3}, Carilli & Walter 2013) where the star formation may occur.

In the right-hand panel of Fig. 4, we plot the [C II] luminosity as a function of $L_{\rm FIR}$ in the case that Gal−A was a [C II] emitter at $z \sim 4.6$, along with other results in the literature for different types of objects (e.g. Malhotra et al. 2001b, Stacey et al. 2010). Our source perfectly sits on the local SFGs relation, with $\log(L_{\rm [C\,II]}/L_{\rm FIR}) \sim -2.5$; possibly, this galaxy may belong to the high-redshift SFGs population which extends to $\log(L_{\rm FIR}/{\rm L}_\odot) \sim 11$. As previously said, the [C II] line is mostly produced by the UV radiation field in star-forming regions (e.g. Cormier et al. 2015), and so it can trace the SFR. As the FIR emission marks out the SFR of a source, the relation

[2]We scale the SFR from Salpeter to Chabrier IMF by dividing by 1.7 (e.g. Zahid et al. 2012).

Table 2. Summary of the physical parameters estimated for the three possible emission lines attributed to Gal−A. The first three columns report the considered emission line, its rest-frequency emission, and the redshift z_{gal} derived using the observed peak frequency, respectively. The fourth and fifth columns list the line luminosity (L_{line}) and the total infrared luminosity (L_{FIR}) for each emission lines, respectively. Finally, the last column report the SFRs, directly computed from the FIR luminosities following Kennicutt (1998).

	ν_{rest} [GHz]	z_{gal}	log(L_{line}) [$L_\odot$]	log(L_{FIR}) [$L_\odot$]	log(SFR) [$M_\odot$ yr^{-1}]
CO(9−8)	1036.9	2.043	8.04 ± 0.04	11.44 ± 0.50	1.45 ± 0.50
CO(10−9)	1152.0	2.381	8.20 ± 0.04	11.42 ± 0.50	1.43 ± 0.50
[C II]	1900.5	4.577	8.88 ± 0.04	11.38 ± 0.50	1.38 ± 0.50

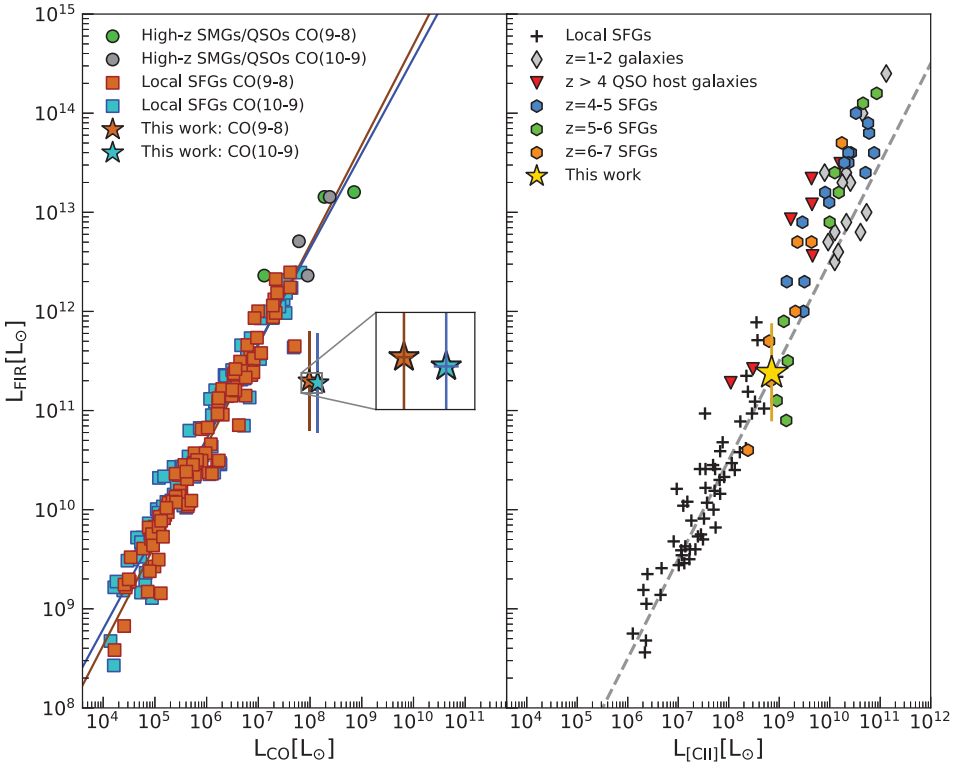

Figure 4. Left-hand panel: empirical relations between CO(9−8) (solid brown line), CO(10−9) (solid blue line) and FIR luminosity (Liu et al. 2015) with overlaid the values for individual local galaxies as brown and blue squares, respectively (Liu et al. 2015, private communication). The two stars are the values found for Gal−A in this work (same colour legend). Error bars are estimated by propagating the error of the line flux on L_{CO}, and assuming a variation of 0.5 dex for L_{FIR}. Also shown are the values obtained for high-redshift SMGs/quasi-stellar objects (QSOs) as the green and grey filled circles in case of CO(9−8) and CO(10−9) transitions, respectively (Carilli & Walter 2013; ALMA Partnership et al. 2015; Carniani et al. 2019). Right-hand panel: [C II] as a function of FIR luminosity for several kinds of objects at different redshifts. Black crosses are local SFGs (Malhotra et al. 2001b); grey diamonds are $z = 1$–2 galaxies, including starburst- and AGN-dominated sources (Stacey et al. 2010); red triangles are $z = 4.1$–7.1 QSO host galaxies (Pety et al. 2004; Maiolino et al. 2005; Iono et al. 2006; Maiolino et al. 2009; Wagg et al. 2010; Willott, Omont & Bergeron 2013); $z = 4$–7 SFGs are the cyan, green, and orange hexagons (Lagache, Cousin & Chatzikos 2018). The dashed grey line represents the average [C II]/FIR ratio for local galaxies (Ota et al. 2014). The yellow star shows the position of our source. Error bars are estimated by propagating the error of the line flux on $L_{[C II]}$, and assuming a variation of 0.5 dex for L_{FIR}.

between the [C II] luminosity and L_{FIR} translates into a correlation between $L_{[C II]}$ and the SFR of a galaxy. Gal−A follows this relation, not showing the typical [C II] deficit which arises at $L_{FIR} > 10^{11}$ $L_\odot$ (e.g. Luhman et al. 1998; Malhotra 2001a; Luhman et al. 2003; Lagache et al. 2018).

These results suggest that our source, randomly detected in the DC_665626 field, may more likely be a strongly obscured [C II] emitter at high redshift. However, to validate this hypothesis, more data are needed.

For the sake of simplicity, in the next sections we adopt an intermediate CO redshift (i.e. $z = 2.2$) between those of the two CO transitions reported in Table 2, as both cases lead to similar results.

3.2 Estimate of the stellar mass

We derive the physical parameters of Gal−A, such as its stellar mass, through SED fitting, comparing the results from the LEPHARE (Arnouts et al. 1999; Ilbert et al. 2006) and the MAGPHYS (da Cunha, Charlot & Elbaz 2008) codes. In the first case, we use a synthetic set of templates of SFGs based on the stellar population synthesis models from Bruzual & Charlot (2003). We explore

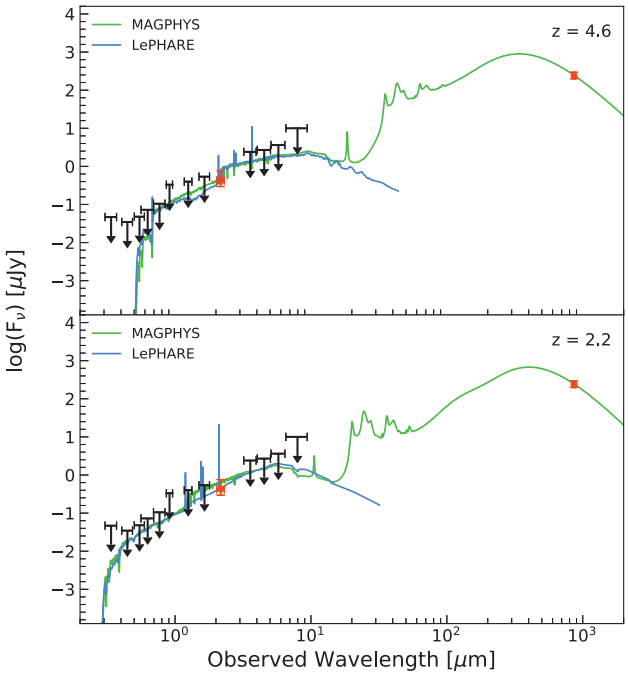

Figure 5. SEDs of Gal−A at $z = 4.6$ (top panel) and $z = 2.2$ (bottom panel). The green and blue curves are the best-fitting models computed with the MAGPHYS and LEPHARE codes, respectively. Upper limits on the flux, as reported in Table 1, are shown in black. The orange points with the error bars are the detection in the UltraVISTA K_s band and the observed ALMA continuum in Band 7.

constant, exponentially declining (with $\tau = 0.1$, 0.3, 1, and 3 Gyr) and delayed (with $\tau = 0.1$, 0.5, 1, and 3 Gyr) SFHs. To account for the metallicity dependence, we use models with solar ($Z_\odot$) and subsolar (0.2 $Z_\odot$) metallicity. We then account for the dust attenuation using the Calzetti et al. (2000) attenuation law with a stellar $E_s(B-V)$ ranging from 0 to 0.7 in steps of 0.05. Following Ilbert et al. (2009), we also add the contribution of the rest-frame UV and optical emission lines in the different filters. However, we note that our final results do not change significantly if we choose not to include the contribution of the emission lines to the SED-fitting process. Finally, we perform the fit in the flux density space and add systematic errors (depending on the filter) in order to avoid the χ^2 computation to be dominated by small errors (Faisst et al. 2019).

Fig. 5 shows the SEDs obtained with LEPHARE (blue curves) from the best fit between the models and the photometry of Gal−A (Table 1) at $z = 4.6$ and 2.2. As Gal−A is very faint from the observed optical to the NIR wavelengths, we decide to perturb the flux in each filter by its relative rms to test the dependence of the fitting on the observed photometry of the galaxy. We thus run a Monte Carlo simulation, building 1000 perturbed SEDs that we then refit, in order to obtain a better estimate of the above-mentioned physical parameters from their probability distributions. More in detail, we extract the perturbed flux in each band from a Gaussian distribution centred on the measured flux and with a standard deviation equal to the measured rms. We list our results in Table 3. At $z = 4.6$, these results point towards the solution for which Gal−A is a young, dusty SFG. Moreover, the SFR and the FIR luminosity are quite in agreement with the corresponding quantities in Table 2. Adopting the same procedure for the SED fitting at $z = 2.2$, we find that Gal−A should be a less massive galaxy but, as expected, with a high level of dust obscuration.

Table 3. Comparison of the physical parameters of Gal−A estimated from the SED fitting at $z = 2.2$ and 4.6 with LEPHARE and MAGPHYS. Each value represents the mean of the probability distribution obtained by perturbing the photometry of Gal−A 1000 times and fitting that photometry with the models. The uncertainties are given by the 16th and 84th percentiles of the distributions.

Physical parameters	$z = 2.2$		$z = 4.6$	
	LEPHARE	MAGPHYS	LEPHARE	MAGPHYS
$E_s(B-V)$	$0.5^{+0.1}_{-0.1}$	$0.6^{+0.2}_{-0.1}$	$0.4^{+0.1}_{-0.1}$	$0.3^{+0.1}_{-0.1}$
log(Age/yr)	$8.0^{+0.4}_{-0.3}$	$8.3^{+0.4}_{-0.5}$	$7.9^{+0.3}_{-0.2}$	$8.0^{+0.2}_{-0.3}$
log(SFR/M$_\odot$ yr^{-1})	$1.5^{+0.3}_{-0.5}$	$1.4^{+0.4}_{-0.4}$	$2.2^{+0.3}_{-0.5}$	$2.0^{+0.1}_{-0.1}$
log(M_*/M$_\odot$)	$9.2^{+0.3}_{-0.2}$	$9.7^{+0.3}_{-0.3}$	$9.9^{+0.2}_{-0.2}$	$10.1^{+0.2}_{-0.2}$
log($L_{\rm FIR}$/L$_\odot$)	$11.1^{+0.1}_{-0.1}$	$11.2^{+0.7}_{-0.5}$	$11.9^{+0.1}_{-0.1}$	$11.9^{+0.2}_{-0.2}$

We then compare the results from the SED fitting by LEPHARE with those obtained with the MAGPHYS code, in which we also include the observed ALMA continuum in Band 7. This code is based on the energy balance between the emission by the stellar populations and the emission and attenuation by the dust in the galaxies. In particular, we use the updated version of the MAGPHYS code which is optimized for the SED fitting of high-redshift ($z > 1$) SFGs (da Cunha et al. 2015). The best models that fit the observations are shown in Fig. 5 as the green curves. At first glance, it is evident that the SEDs reproduced by LEPHARE and MAGPHYS are quite similar to each other at both redshifts. This is confirmed by the physical parameters of our galaxy obtained with MAGPHYS after perturbing the photometry 1000 times. These parameters are listed in Table 3, along with those computed with LEPHARE. The results from the two codes are in good agreement within the uncertainties, both at $z = 2.2$ and 4.6. This reassures us about the robustness of our estimates.

Hereafter, as our conclusions do not change if considering the outputs from one or the other code, we decide to use the physical parameters estimated with LEPHARE in order to make consistent comparisons to other works.

With the stellar mass obtained from the SED fitting (i.e. $\log(M_*/M_\odot) \sim 9.9$) and the SFRs measured from the FIR luminosity of the source (i.e. $\log(\mathrm{SFR}/M_\odot\ \mathrm{yr}^{-1}) \sim 1.4$), we determine the position of Gal−A along the MS of SFGs (given the large uncertainties involved, our conclusions do not change if using the SFRs from the SED fitting). In Fig. 6, we show the MS relations, assuming a Chabrier IMF, at $z = 2.2$ (left-hand panel) and $z = 4.6$ (right-hand panel), as obtained by Speagle et al. (2014) by combining measurements from previous works in the literature. Should the source be at $z = 2.2$, it would lie $\sim 2\sigma$ above the MS, towards the region populated by starburst galaxies. Whether the source is at $z = 4.6$, instead, it would sit on its corresponding MS. In this case, we also show the location of the ALPINE sample (in the redshift range $4.4 \leq z \leq 4.6$) in the figure. The ALPINE galaxies have ages in the range $7.8 \lesssim \log(\mathrm{Age/yr}) \lesssim 9.0$ and $E_s(B-V)$ between 0 and 0.5 (Faisst et al. 2019). Gal−A has a similar age to those estimated for the ALPINE targets. Moreover, its SFR and M_* are comparable with those of the ALPINE sources and place it along the MS at $z = 4.6$. However, the mean $E_s(B-V)$ of the ALPINE galaxies is $\sim$0.1, while Gal−A has $E_s(B-V) \sim 0.4$, lying on the tail of the distribution of the colour excess, and making it undetected in the optical bands. In this scenario, we should expect an entire

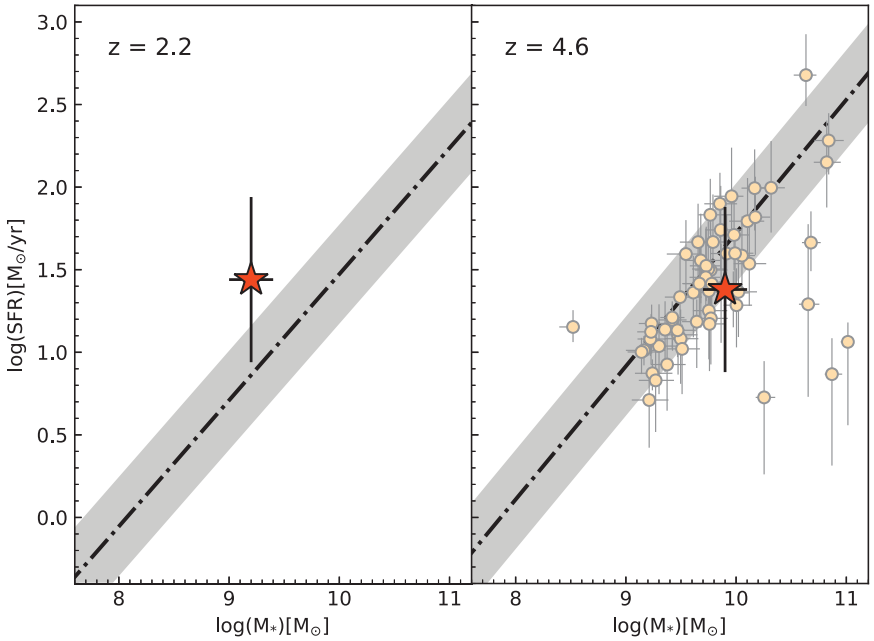

Figure 6. Star-forming MS relations (dotted–dashed lines; Speagle et al. 2014) at redshift 2.2 (left-hand panel) and 4.6 (right-hand panel). The grey bands indicate the scatter from the MS (±0.3 dex width). The orange stars represent the positions of our source in the diagram, given by the estimated stellar mass from the SED fitting with LEPHARE and the SFR from the FIR luminosity of Gal−A. For the case at $z = 4.6$, we also show the positions of the ALPINE galaxies at $4.4 \leq z \leq 4.6$ (small circles).

population of optically invisible SFGs still to be observed, which might contribute to the cosmic SFRD at early times.

3.3 Estimate of the dynamical mass

In this paragraph, we attempt an estimate of the galaxy dynamical mass ($M_{\rm dyn}$) obtained from the FWHM of the observed emission line. Following Wang et al. (2013), we assume a rotating disc geometry for the gas as a first approximation. In this way, $M_{\rm dyn} = 1.16 \times 10^5\, v_{\rm cir}^2\, D$, where $v_{\rm cir} = 0.75\ {\rm FWHM_{line}}\ \sin^{-1}(i)$ is the circular velocity of the gas disc in km s^{-1} (with i the inclination angle between the gas disc and the line of sight) and D is the disc diameter in kpc. Since Gal−A is not resolved, we take the FWHM of the major axis of the 2D Gaussian fitted to the emission line as the size of our galaxy (1.06 ± 0.04 arcsec, which corresponds to 7.09 ± 0.27 kpc at $z \sim 4.6$, and to 8.99 ± 0.34 kpc at $z \sim 2.2$). We derive dynamical masses (uncorrected for the galaxy inclination) of $M_{\rm dyn}\ \sin^2(i) = 4.4 \times 10^{10}$ and 5.6×10^{10} M$_\odot$ for $z = 4.6$ and 2.2 respectively, with a 25 per cent of uncertainty obtained from the individual errors on the FHWM$_{\rm line}$ and on the size of the source. Following Capak et al. (2015), we assume as values for the inclination angle $\sin(i) = 0.45$ and 1, ranging from a nearly face-on to an edge-on disc. When $\sin(i) = 1$, the previous dynamical masses remain unchanged. However, in the case with $\sin(i) = 0.45$, $M_{\rm dyn}$ increases of a factor 5. This reflects the large uncertainties on the size and geometry of the source, which cannot be well constrained with the current data and our poor resolution.

Furthermore, this approximation could cease to be valid in the case that the stellar mass of the source is smaller than the mass threshold above which the galaxies are thought to form ordered discs. For instance, Simons et al. (2015) found a so-called mass of disc formation of $\log(M_*/{\rm M}_\odot) = 9.5$ above which the majority of the galaxies of their sample are rotation-dominated. Below this threshold, there is instead a large scatter and the galaxies could be either rotation-dominated discs and asymmetric or compact galaxies without any sign of rotation. At $z = 2.2$, Gal−A should have $\log(M_*/{\rm M}_\odot) = 9.2$, therefore it is prone to this kind of issue.

For comparison, we also run the 3D-BAROLO algorithm (3D-Based Analysis of Rotating Objects from Line Observations, Di Teodoro & Fraternali 2015) on the continuum-subtracted data cube to obtain a more accurate estimate of the dynamical mass. This code creates synthetic 3D observations of the galaxy and compares them with the input data cube, finding the kinematical and geometrical parameters which best describe the data. It is particularly useful to retrieve information on low-resolution data where the kinematics is biased by the size of the beam, as in this case. We find $\log(M_{\rm dyn}/{\rm M}_\odot) = 10.4 \pm 1.0$ for $z = 4.6$ and $\log(M_{\rm dyn}/{\rm M}_\odot) = 10.5 \pm 1.0$ for $z = 2.2$. These results are quite in agreement with the former, given the large error on $M_{\rm dyn}$. As a result, at both redshifts $M_{\rm dyn}/M_* > >1$, likely indicating that the galaxy has recently begun forming stars, resulting in small stellar masses and large gas fractions. In particular, in the case that our galaxy is a [C II] emitter at $z = 4.6$, we estimate the fraction of molecular gas as $f_{\rm mol} = M_{\rm mol}/(M_{\rm mol} + M_*)$, where $M_{\rm mol}$ is the molecular gas mass. Following Zanella et al. (2018), which found a tight correlation between the [C II] luminosity and the molecular gas mass (Dessauges-Zavadsky et al. 2020), we derive $\log(M_{\rm mol}/{\rm M}_\odot) \sim 10.4$. Assuming a small contribution of the dark matter in the galaxy (e.g. Barnabè et al. 2012), this value is comparable with the gas mass resulting from the subtraction of the stellar mass from the dynamical mass. We thus obtain $f_{\rm mol} \sim 0.75$ that is in perfect agreement with the average molecular gas fraction estimated for the ALPINE targets at $z \sim 4.5$ (Dessauges-Zavadsky et al. 2020). However, given the large uncertainties involved in the computation of the dynamical mass, this result is not conclusive.

4 DISCUSSION

From the [C II]/FIR diagnostic, our source presents similar properties to a large population of SFGs in the literature. The SED fitting reveals a large dust attenuation as expected for such an obscured galaxy and places Gal−A along the MS at $z \sim 4.6$. In addition, we compute the rest-frame equivalent width (EW) of the [C II] line as the ratio between the flux of the [C II] emission and the flux density of the underlying continuum, that is $EW_{[C\,II]} \sim 0.46$ μm. This result is in agreement with the EW estimated for the high-redshift SMGs in Swinbank et al. (2012) identified as [C II] emitters at $z \sim 4.4$ and with the median EW of the candidates [C II] emitters at $z \sim 4.5$ in Cooke et al. (2018). We also compare the observed photometry of our source with that of a sample of ∼700 SMGs from the AS2UDS survey in Dudzevičiūtė et al. (2020), where they show how the observed *K*-band magnitude decreases with the redshift (see their fig. 5). We find that Gal−A follows very well the observed trend. In particular, the estimated K_s magnitude sets our galaxy on the composite SMG SED they obtain by measuring the median value of each individual SED at different wavelengths. The set of the above results strongly suggests that Gal−A is a dust-obscured galaxy at $z \sim 4.6$.

Nevertheless, we cannot exclude the possibility that the observed emission line is associated to a dusty, less massive source at $z \sim 2.2$, with a $\sim 2\sigma$ scatter from the MS and with implied CO luminosities that are a factor about 10 or more higher than the typical CO luminosities of local SFGs or high-z SMGs and QSOs. In this latter case, the (spectroscopic) redshift of Gal−A would also be comparable with the (photometric) redshifts of Gal−B and Gal−C, maybe suggesting the presence of an ongoing merging at that epoch. However, to test this hypothesis, more kinematic information is needed.

In the most likely scenario in which Gal−A is at $z \sim 4.6$, it may be part of the same dark matter halo of DC_665626. In this case, we can assume a stellar mass–halo mass (SMHM) relationship in order to estimate some physical properties of the halo. There are several ways to derive this relation. For instance, Behroozi, Conroy & Wechsler (2010) and Behroozi, Wechsler & Conroy (2013) used the abundance matching technique to explore the SMHM relation out to $z \sim 8$, assuming that the most massive galaxies are monotonically assigned to the most massive haloes. Another frequent approach is the halo occupation distribution modelling which assumes that the number of galaxies in a given dark matter halo depends only on the halo mass. Harikane et al. (2016) used this method to reproduce the SMHM relation out to $z = 7$, obtaining results in agreement with Behroozi et al. (2013). In particular, since Gal−A has a larger stellar mass than DC_665626, we can suppose that the ALPINE target is a satellite galaxy of our serendipitous source embedded in its dark matter halo. In this case, from the stellar mass of Gal−A (i.e. $\log(M_*/M_\odot) = 9.9 \pm 0.2$), the previously discussed models predict a halo mass between $\log(M_H/M_\odot) \sim 11.5$ and ~ 11.7. Using the empirical model by Mashian, Oesch & Loeb (2015), which links the SFR of the central galaxy to its host halo mass via abundance matching techniques, M_H also translates into an SFR between ∼20 and 40 $M_\odot$ yr^{-1}, in agreement within the uncertainties with the value estimated from the FIR continuum for Gal−A, that is SFR ∼24 $M_\odot$ yr^{-1}. Exploiting this information and following Lapi et al. (2018), we compute the virial radius of the halo as $R_H \equiv [3M_H/4\pi\,\rho_c\,\Delta_H E_z]^{1/3}$, where $\rho_c \approx 2.8 \times 10^{11}$ h^2 $M_\odot$ Mpc^{-3} is the critical density, $\Delta_H \simeq 18\pi^2 + 82[\Omega_m(1+z)^3/E_z - 1] - 39[\Omega_m(1+z)^3/E_z - 1]^2$ is the non-linear density contrast at the collapse, and $E_z = \Omega_\Lambda + \Omega_m(1+z)^3$ is a redshift-dependent factor; we obtain $R_H \sim 39$–45 kpc. Comparing this result to the observed spatial offset between our source and DC_665626 (∼40 kpc), we may conclude, according to this scenario, that the main ALPINE target could be a low-mass satellite in the dark matter halo of Gal−A.

It is worth noting that we obtain similar results even in the opposite case in which Gal−A is a satellite galaxy of DC_665626. Following the same procedure explained above and since DC_665626 has $\log(M_*/M_\odot) \sim 9.2$, we obtain $\log(M_H/M_\odot) \sim 11.4$ and $\log(SFR/M_\odot\ yr^{-1}) \sim 1.0$ (which is consistent with the SFR of the ALPINE target obtained through the SED fitting). In turn, this provides $R_H \sim 36$ kpc, which is again comparable with the observed offset between the two galaxies.

Finally, Gal−A may also be part of the massive protocluster of galaxies PCI J1001+0220 located at $z = 4.57$ in the COSMOS field (Lemaux et al. 2018). In fact, our source lies well inside the 2 Mpc boundary used for spectroscopic membership in that work, with a systemic velocity offset <350 km s^{-1}. This strengthens the hypothesis that this source is at $z \sim 4.6$.

5 SUMMARY AND CONCLUSIONS

In this paper, we present the characterization of a heavily dust-obscured galaxy, named Gal−A, serendipitously discovered in one of the ALPINE pointings. This source is detected both in line and continuum emissions and does not show any associated counterpart, from the UV to the FIR wavelengths, except for the K_s band from UltraVISTA (DR4). This leads to high uncertainties on the real nature of the observed emission line, that is [C II] at $z_{gal} = 4.577$, CO(9−8) or CO(10−9) at $z_{gal} = 2.043$ and 2.381, respectively.

Although we cannot definitively exclude that Gal−A is a dust-obscured galaxy at $z \sim 2.2$, the analysis undertaken in this work suggests that this source is more likely a $z \sim 4.6$ MS SFG missed by the UV/optical surveys because of its high level of dust obscuration. There is much evidence in favour of this latter scenario:

(i) The observed emission line has a relatively high rest-frame EW, that is $EW_{[C\,II]} \sim 0.46$ μm, compatible with other [C II] emitters at similar redshifts (e.g. Swinbank et al. 2012; Cooke et al. 2018).

(ii) The [C II]/FIR ratio places our source right on the local SFGs relation (Ota et al. 2014), also among several high-redshift SFGs. At the same time, the estimated CO luminosities for Gal−A are more than 10 times larger (at fixed L_{FIR}) than the typical luminosities of high-J CO transitions for local SFGs and high-z SMGs and QSOs (e.g. Liu et al. 2015; Carilli & Walter 2013), disfavouring the $z \sim 2.2$ case.

(iii) This galaxy is detected in the K_s band of the UltraVISTA survey with an AB magnitude of ∼24.4. This value exactly follows the expected trend with redshift of the composite SED of the SMG sample analysed by Dudzevičiūtė et al. (2020). Exploiting the available photometry of Gal−A, we thus obtain $\log(Age/yr) \sim 7.9$ and $\log(M_*/M_\odot) \sim 9.9$. These results, together with $\log(SFR/M_\odot\ yr^{-1}) \sim 1.4$ (estimated from the observed FIR luminosity), place Gal−A on the $z \sim 4.6$ MS, along with the rest-frame UV-selected ALPINE targets.

(iv) Our galaxy may be part of a massive protocluster, that is PCI J1001+0220, recently discovered at $z \sim 4.57$ in the COSMOS field (Lemaux et al. 2018). In fact, Gal−A lies at only ∼1 proper Mpc from the centre of the overdensity, with a spectroscopic redshift close to that of the systemic redshift of the protocluster.

(v) At this epoch, several dust-obscured galaxies without optical/NIR detections have been already confirmed, mostly as starbursts/SMGs (e.g. Swinbank et al. 2012; Riechers et al. 2013;

Simpson et al. 2014; Riechers et al. 2017; Cooke et al. 2018; Alcalde Pampliega et al. 2019). Gal−A could be part of this elusive population of sources likely being an MS galaxy with less extreme properties, such as a smaller mass and/or luminosity.

Whether the emission comes from CO or [C II], both the cases presented above are undoubtedly interesting. If it was at $z \sim 2.2$, our galaxy would increase the sample of high-J CO emitters at high redshift, leading to a more in-depth study of the excitation conditions of the molecular gas in these sources. Only a handful of these kind of objects has been detected so far and most of them seem to be associated with active galactic nuclei (AGNs) activities (Weiß et al. 2007; Riechers et al. 2011, 2013). Should the serendipitous emission be [C II] instead, we would identify an SFG invisible to optical/NIR observations.

As found in Loiacono et al. (2020), a large fraction (∼57 per cent) of the serendipitous sources found in ALPINE is confirmed to be [C II] emission at $z > 4$, with an additional ∼29 per cent of objects (including our galaxy) showing no counterparts and considered as promising [C II] candidates. Only ∼14 per cent of the sources are confirmed to be CO emitters at lower redshift. In particular, using the global sample of [C II] emitters (both confirmed and candidates), they obtain a cosmic SFRD which is ∼2 times higher than the previous estimates from the UV surveys (if considering their results for the average galaxy population at $z \sim 5$; see their upcoming work for more details). This result stands out the large contribution of the obscured star formation in the early Universe and the importance of searching for elusive sources, as the one analysed in this work.

Eventually, we plan to spectroscopic follow-up this source in order to firmly establish the nature of its emission line. For instance, ALMA observations in Band 6 could reveal [N II] emission at 205 μm rest frame if the galaxy is at $z \sim 4.6$; in this case the ratio [C II]/[N II] would also provide the fraction of [C II] emission arising from the ionized gas, that is from star-forming regions (Oberst et al. 2006, 2011; Zhao et al. 2010). X-shooter at the VLT could also be useful to unveil the redshift of this source by observing the [O II] emission at $z = 4.6$, or even the Hα emission redshifted in the NIR region of the spectrum at $z \sim 2.2$. However, these observations could be hampered by the large $E_s(B-V)$ found for this source which makes it invisible in the optical filters. Finally, the Near-Infrared Spectrograph on the *James Webb Space Telescope* will be a powerful facility for the follow-up of this kind of sources as well.

ACKNOWLEDGEMENTS

This paper is based on data obtained with the ALMA observatory, under the Large Program 2017.1.00428.L. ALMA is a partnership of ESO (representing its member states), NSF (USA) and NINS (Japan), together with NRC (Canada), MOST and ASIAA (Taiwan), and KASI (Republic of Korea), in cooperation with the Republic of Chile. The Joint ALMA Observatory is operated by ESO, Associated Universities,Inc. (AUI)/National Radio Astronomy Observatory (NRAO) and NAOJ. Based on data products from observations made with ESO Telescopes at the La Silla Paranal Observatory under ESO programme ID 179.A-2005 and on data products produced by CALET and the Cambridge Astronomy Survey Unit on behalf of the UltraVISTA consortium. This work has made use of the Rainbow Cosmological Surveys Database, which is operated by the Centro de Astrobiología (CAB/INTA), partnered with the University of California Observatories at Santa Cruz (UCO/Lick,UCSC). We thank D. Liu and collaborators for providing us individual values of CO and FIR luminosities estimated in their work. SB, AC, CG, FL, FP, GR, and MT acknowledge the support from grant PRIN MIUR 2017. LV acknowledges funding from the European Union's Horizon 2020 research and innovation program under the Marie Sklodowska-Curie grant agreement no. 746119. DR acknowledges support from the National Science Foundation under grant numbers AST-1614213 and AST-1910107 and from the Alexander von Humboldt Foundation through a Humboldt Research Fellowship for Experienced Researchers. GCJ acknowledges ERC Advanced grant 695671 'QUENCH' and support by the Science and Technology Facilities Council (STFC). SF is supported by the Cosmic Dawn Center of Excellence founded by the Danish National Research Foundation under the grant no. 140. EI acknowledges partial support from FONDECYT through grant number 1171710. JDS was supported by JSPS KAKENHI grant number JP18H04346, and the World Premier International Research Center Initiative (WPI Initiative), MEXT, Japan.

REFERENCES

Alcalde Pampliega B. et al., 2019, ApJ, 876, 135
ALMA Partnership et al., 2015, ApJ, 808, 4
Álvarez-Márquez J. et al., 2016, A&A, 587, 122
Aravena M. et al., 2016, ApJ, 833, 71
Arnouts S., Cristiani S., Moscardini L., Matarrese S., Lucchin F., Fontana A., Giallongo E., 1999, MNRAS, 310, 540
Barnabè M. et al., 2012, MNRAS, 423, 1073
Barro G. et al., 2011a, ApJS, 193, 13
Barro G. et al., 2011b, ApJS, 193, 30
Behroozi P. S., Conroy C., Wechsler R. H., 2010, ApJ, 717, 379
Behroozi P. S., Wechsler R. H., Conroy C., 2013, ApJ, 770, 57
Bertin E., Arnouts S., 1996, A&AS, 117, 393
Béthermin M. et al., 2020, A&A, accepted
Blain A. W., Smail I., Ivison R. J., Kneib J. -P., Frayer D. T., 2002, Phys. Rep., 369, 111
Bouwens R. J. et al., 2011, Nature, 469, 504
Bouwens R. J. et al., 2012a, ApJ, 754, 83
Bouwens R. J. et al., 2012b, ApJ, 752, 5
Bouwens R. J. et al., 2016, ApJ, 833, 72
Bradač M. et al., 2017, ApJ, 836, 2
Bruzual G., Charlot S., 2003, MNRAS, 344, 1000
Calzetti D., Armus L., Bohlin R. C., Kinney A. L., Koornneef J., Storchi-Bergmann T., 2000, ApJ, 533, 682
Capak P. L. et al., 2007, ApJS, 172, 99
Capak P. L. et al., 2008, ApJ, 681, 53
Capak P. L. et al., 2015, Nature, 522, 455
Cardamone C. N. et al., 2010, ApJS, 189, 270
Carilli C. L., Walter F., 2013, ARA&A, 51, 105
Carniani S. et al., 2019, MNRAS, 489, 3939
Casey C. M. et al., 2012, ApJ, 761, 140
Casey C. M., Narayanan D., Cooray A., 2014, Phys. Rep., 541, 45
Casey C. M., Hodge J., Zavala J. A., Spilker J., da Cunha E., Staguhn J., Finkelstein S. L., Drew P., 2018, ApJ, 862, 68
Cassata P. et al., 2020, preprint (arXiv:2002.00967)
Castellano M. et al., 2014, A&A, 566, 19
Chabrier G., 2003, PASP, 115, 763
Cooke E. A. et al., 2018, ApJ, 861, 100
Cormier D. et al., 2012, A&A, 548, 20
Cormier D. et al., 2015, A&A, 578, 53
da Cunha E., Charlot S., Elbaz D., 2008, MNRAS, 388, 1595
da Cunha E. et al., 2015, ApJ, 806, 110
Daddi E. et al., 2007, ApJ, 670, 156
Daddi E. et al., 2009, ApJ, 694, 1517
De Looze I. et al., 2014, A&A, 568, 62
Dessauges-Zavadsky M. et al., 2020, preprint (arXiv:2004.10771)
Di Teodoro E. M., Fraternali F., 2015, MNRAS, 451, 3021
DudzevičiūtėU. et al., 2020, MNRAS, 494, 3828

Dunlop J. S. et al., 2004, MNRAS, 350, 769
Faber S. M. et al., 2003, in Iye M., Moorwood A. F. M., eds, Proc. SPIE Conf. Ser., Vol. 4841, Instrument Design and Performance for Optical/Infrared Ground-based Telescopes. SPIE, Bellingham, p. 1657
Faisst A. L. et al., 2019, ApJS, 247, 61
Gallerani S. et al., 2010, A&A, 523, 85
Gallerani S. et al., 2012, A&A, 543, 114
Genzel R. et al., 2015, ApJ, 800, 20
Giavalisco M., 2002, ARA&A, 40, 579
Giavalisco M. et al., 2004, ApJ, 600, 93
Harikane Y. et al., 2016, ApJ, 821, 123
Hasinger G. et al., 2018, ApJ, 858, 77
Hodge J. A. et al., 2013, ApJ, 768, 91
Hollenbach D. J., Tielens A. G. G. M., 1999, Rev.Mod. Phys., 71, 173
Huang J.-S. et al., 2014, ApJ, 784, 52
Ilbert O. et al., 2006, A&A, 457, 841
Ilbert O. et al., 2009, ApJ, 690, 1236
Ilbert O. et al., 2013, A&A, 556, 55
Iono D. et al., 2006, ApJ, 645, 97
Kaufman M. J., Wolfire M. G., Hollenbach D. J., Luhman M. L., 1999, ApJ, 527, 795
Kennicutt R. C., 1998, ARA&A, 36, 189
Koekemoer A. M. et al., 2007, ApJS, 172, 196
Koekemoer A. M. et al., 2011, ApJS, 197, 36
Lagache G., Cousin M., Chatzikos M., 2018, A&A, 609, 130
Laigle C. et al., 2016, ApJS, 224, 24
Lapi A. et al., 2018, ApJ, 857, 22
Le Fèvre O. et al., 2003, in Iye M., Moorwood A. F. M., eds, Proc. SPIE, Vol. 4841, Instrument Design and Performance for Optical/Infrared Ground-based Telescopes. SPIE, Bellingham, p. 1670
Le Fèvre O. et al., 2015, A&A, 576, 79
Le Fèvre O. et al., 2019, A&A, accepted
Lemaux B. C. et al., 2018, A&A, 615, 77
Lilly S. J., Le Fèvre O., Hammer F., Crampton D., 1996, ApJ, 460, 1
Liu D., Gao Y., Isaak K., Daddi E., Yang C., Lu N., van der Werf P., 2015, ApJ, 810, 14
Loiacono F., et al., 2020, A&A, preprint (arXiv:2006.04837)
Luhman M. L. et al., 1998, ApJ, 504, 11
Luhman M. L., Satyapal S., Fischer J., Wolfire M. G., Sturm E., Dudley C. C., Lutz D., Genzel R., 2003, ApJ, 594, 758
Madau P., Dickinson M., 2014, ARA&A, 52, 415
Madden S. C., Poglitsch A., Geis N., Stacey G. J., Townes C. H., 1997, ApJ, 483, 200
Magdis G. E. et al., 2012, ApJ, 760, 6
Maiolino R. et al., 2005, A&A, 440, 51
Maiolino R., Caselli P., Nagao T., Walmsley M. De Breuck C., Meneghetti M., 2009, A&A, 500, 1
Maiolino R. et al., 2015, MNRAS, 452, 54
Malhotra S., 2001, in Pilbratt G. L., Cernicharo J., Heras A. M., Prusti T., Harris R., eds, The Promise of the Herschel Space Observatory, Far Infrared Spectroscopy of Star-Forming Galaxies: Expectations for the Herschel Space Observatory, 460, p. 155
Malhotra S. et al., 2001, ApJ, 561, 766
Mashian N., Oesch P., Loeb A., 2015, MNRAS, 455, 2101
McCracken H. J. et al., 2012, A&A, 544, 156
McMullin J. P., Waters B., Schiebel D., Young W., Golap K., 2007, in Shaw R. A., Hill F., Bell D. J., eds, ASP Conf. Ser., Vol. 376, Astronomical Data Analysis Software and Systems XVI. Astron. Soc. Pac., San Francisco, p. 127
Naab T., Ostriker J. P., 2017, ARA&A, 55, 59
Novak M. et al., 2017, A&A, 602, 5
Oberst T. E. et al., 2006, ApJ, 652, 125
Oberst T. E., Parshley S. C., Nikola T., Stacey G. J., Löhr A., Lane A. P., Stark A. A., Kamenetzky J., 2011, ApJ, 739, 100
Oesch P. A., Bouwens R. J., Illingworth G. D., Franx M., Ammons S. M., van Dokkum P. G., Trenti M., Labbé I., 2015, ApJ, 808, 104
Ota K. et al., 2014, ApJ, 792, 34
Pavesi R. et al., 2016, ApJ, 832, 151
Pavesi R. et al., 2018, ApJ, 861, 43
Peng C. Y., Ho L. C., Impey C. D., Rix H.-W., 2002, AJ, 124, 266
Pérez-González P. G. et al., 2008, ApJ, 675, 234
Pety J., Beelen A., Cox P., Downes D., Omont A., Bertoldi F., Carilli C. L., 2004, A&A, 428, 21
Planck Collaboration, 2018, preprint (arXiv:1807.06209)
Renzini A., 2006, ARA&A, 44, 141
Riechers D. A. et al., 2010, ApJ, 720, 131
Riechers D. A., Walter F., Carilli C. L., Cox P., Weiss A., Bertoldi F., Menten K. M., 2011, ApJ, 726, 50
Riechers D. A. et al., 2013, Nature, 496, 329
Riechers D. A. et al., 2017, ApJ, 850, 1
Rodighiero G. et al., 2011, ApJ, 739, 40
Santini P. et al., 2016, A&A, 596, 75
Santini P. et al., 2017, ApJ, 847, 76
Schenker M. A. et al., 2013, ApJ, 768, 196
Scoville N. et al., 2007, ApJS, 172, 1
Scoville N. et al., 2007, ApJS, 172, 38
Scoville N., Faisst A., Capak P., Kazaku Y., Li G., Steinhardt C., 2015, ApJ, 800, 108
Scoville N. et al., 2016, ApJ, 820, 83
Silk J., Mamon G. A., 2012, Res. Astron. Astrophys., 12, 917
Silverman J. D. et al., 2015, ApJ, 812, 23
Simons R. C., Kassin S. A., Weiner B. J., Heckman T. M., Lee J. C., Lotz J. M., Peth M., Tchernyshyov K., 2015, MNRAS, 452, 986
Simpson J. M. et al., 2014, ApJ, 788, 125
Solomon P. M., Downes D., Radford S. J. E., 1992, ApJ, 398, 29
Speagle J. S., Steinhardt C. L., Capak P. L., Silverman J. D., 2014, ApJS, 214, 15
Stacey G. J., Geis N., Genzel R., Lugten J. B., Poglitsch A., Sternberg A., Townes C. H., 1991, ApJ, 373, 423
Stacey G. J., Hailey-Dunsheath S., Ferkinhoff C., Nikola T., Parshley S. C., Benford D. J., Staguhn J. G., Fiolet N., 2010, ApJ, 724, 957
Swinbank A. M. et al., 2012, MNRAS, 427, 1066
Vallini L., Gallerani S., Ferrara A., Baek S., 2013, MNRAS, 433, 1567
Vallini L., Gallerani S., Ferrara A., Pallottini A., Yue B., 2015, ApJ, 813, 36
Wagg J., Carilli C. L., Wilner D. J., Cox P., De Breuck C., Menten K., Riechers D. A., Walter F., 2010, A&A, 519, 1
Walter F. et al., 2012, Nature, 486, 233
Wang R. et al., 2013, ApJ, 773, 44
Wang T. et al., 2016, ApJ, 816, 84
Weiß A, Downes D., Neri R., Walter F., Henkel C., Wilner D. J., Wagg J., Wiklind T., 2007, A&A, 467, 955
Williams C. C. et al., 2019, ApJ, 884, 154
Willott C. J., Omont A., Bergeron J., 2013, ApJ, 770, 13
Willott C. J., Carilli C. L., Wagg J., Wang R., 2015, ApJ, 807, 180
Wolfire M. G., McKee C. F., Hollenbach D., Tielens A. G. G. M., 2003, ApJ, 587, 278
Zahid H. J., Dima G. I., Kewley L. J., Erb D. K., Davé R., 2012, ApJ, 757, 54
Zanella A. et al., 2018, MNRAS, 481, 1976
Zhao Y. et al., 2016, ApJ, 819, 69

[1]*Dipartimento di Fisica e Astronomia, Università di Padova, Vicolo dell'Osservatorio 3, I-35122 Padova, Italy*
[2]*INAF – Osservatorio Astronomico di Padova, Vicolo dell'Osservatorio 5, I-35122 Padova, Italy*
[3]*Department of Physics, University of California, Davis, One Shields Ave., Davis, CA 95616, USA*
[4]*Aix Marseille Université, CNRS, LAM, UMR 7326, 13388, Marseille, France*
[5]*IPAC, California Institute of Technology, 1200 East California Boulevard, Pasadena, CA 91125, USA*
[6]*The Cosmic Dawn Center, University of Copenhagen, Vibenshuset, Lyngbyvej 2, DK-2100 Copenhagen, Denmark*
[7]*Niels Bohr Institute, University of Copenhagen, Lyngbyvej 2, DK-2100 Copenhagen, Denmark*

[8]*Observatoire de Genève, Université de Genève 51 Ch. des Maillettes, CH-1290 Versoix, Switzerland*
[9]*Institut de Recherche en Astrophysique et Planétologie (IRAP), CNRS, Université de Toulouse, UPS-OMP, 14, avenue E. Belin, F-31400 Toulouse, France*
[10]*Kavli Institute for the Physics and Mathematics of the Universe, The University of Tokyo Kashiwa, Chiba 277-8583, Japan*
[11]*Department of Astronomy, School of Science, The University of Tokyo, 7-3-1 Hongo, Bunkyo, Tokyo 113-0033, Japan*
[12]*The Caltech Optical Observatories, California Institute of Technology, Pasadena, CA 91125, USA*
[13]*Istituto Nazionale di Astrofisica, Osservatorio di Astrofisica e Scienza dello Spazio, via Gobetti 93/3, I-40129 Bologna, Italy*
[14]*Centro de Astronomía (CITEVA), Universidad de Antofagasta, Avenida Angamos 601, Antofagasta, Chile*
[15]*Department of Physics and Astronomy (DIFA), University of Bologna, Via Gobetti 93/2, I-40129 Bologna, Italy*
[16]*INAF – Osservatorio Astrofisico di Arcetri, Largo E. Fermi 5, I-50125 Firenze, Italy*
[17]*Niels Bohr Institute, University of Copenhagen, Lyngbyvej 2, DK-2100 Copenhagen, Denmark*
[18]*Space Telescope Science Institute, 3700 San Martin Drive, Baltimore, MD 21218, USA*
[19]*Instituto de Física y Astronomía, Universidad de Valparaíso, Avda. Gran Bretaña 1111, Valparaíso, Chile*
[20]*Cavendish Laboratory, University of Cambridge, 19 J. J. Thomson Ave., Cambridge CB3 0HE, UK*
[21]*Kavli Institute for Cosmology, University of Cambridge, Madingley Road, Cambridge CB3 0HA, UK*
[22]*Department of Astronomy, Cornell University, Space Sciences Building, Ithaca, NY 14853, USA*
[23]*Max-Planck-Institut für Astronomie, Königstuhl 17, D-69117 Heidelberg, Germany*
[24]*Leiden Observatory, Leiden University, P.O. Box 9500, NL-2300 RA Leiden, the Netherlands*

This paper has been typeset from a TEX/LATEX file prepared by the author.